AIAA JOURNAL
Vol. 32, No. 6, June 1994

Numerical Simulation of Vortex-Wedge Interaction

Jin-Ho Park* and Duck-Joo Lee†
Korea Advanced Institute of Science and Technology, Taejon 305-701, Republic of Korea

Interactions between vortical flows and a solid surface cause one of the primary sources of noise and unsteady loading. The mechanism of the interaction is studied numerically for a single Rankine vortex impinging upon a wedge. An Euler-Lagrangian method is employed to calculate the unsteady, viscous, incompressible flows in two dimensions. A random vortex method is used to describe the vorticity dominant field. A fast vortex method is used to reduce the computational time in the calculation of the convection velocity of each vortex particle. A Schwarz-Christoffel transformation is used to map the numerical domain onto the physical domain. Vortex particle plots, velocity vectors, and streamlines are presented at selected times for both inviscid and viscous interactions. It is observed that the incident Rankine vortex distorts and is split by the wedge as it nears and passes the wedge, and the vortices generated from the leading edge toward the underside of the wedge form into a single vortex. The vorticity orientation of the shed vortex is opposite to that of the incident vortex. It is found that the convection velocity of the shed vortex is changed when it comes off the leading edge of the wedge, and the strength of the shed vortex varies with time during the vortex-wedge interaction. This strength variation is presumed to influence the shed vortex convection velocity. The overall features for the interaction agree well with the experimental results of Ziada and Rockwell.[1]

Introduction

UNSTEADY flows induced by vortex-body interaction have been studied by many researchers, as reviewed by Rockwell.[2] These flows cause unsteady loading as well as related noise generation in a number of cases: helicopter rotors, marine propellers, supersonic intakes and cavities, etc. For vortex-wedge interaction, as a vortex nears the leading edge of a wedge, the vortex distorts, and another vortex is shed from the leading edge due to the significant timewise change in the local angle of attack of the flow induced by the nearing vortex.[1]

Vortex-wedge interaction was first studied experimentally by Ziada and Rockwell.[1] In their study, interactions between a row of vortices in the mixing layer and the leading edge of a wedge were investigated. This flow can be considered as a self-sustained shear flow,[2] which has a feedback mechanism between the shear generator and the wedge. Vortex-corner interaction was investigated by Rockwell and Knisely[3] and was simulated by Conlisk and Rockwell[4] with a point vortex interacting with a rectangular corner. Later, the flow and acoustic field are calculated[5] for the various initial positions of point vortices. In the case of vortex-wedge interaction, it was found that the transverse (vertical) position of the incident vortex relative to the centerline of the wedge is important to the interactions[1]; for the vortex initially located above the wedge, a strong nonlinear interaction occurs between the incident vortex and the wedge, and a strong vortex is shed from the leading edge of the wedge.

The point vortex core model,[4] used in the corner interaction, is not adequate for the simulation of the severe distortion of the vortex. The distortion of the incident vortex can be well depicted by modeling the vortex core as multiple vortex elements that are free to move. This was done by the author[6,7] for blade-vortex interaction with the assumption of no separation near the airfoil, that is, inviscid flow. For the case of vortex-wedge interaction, viscous effects should be considered to simulate the leading-edge separation.

In this paper, we simulated a vortex shedding near the leading edge of a wedge as well as the distortion and splitting of an incident vortex, as schematically depicted in Fig. 1. A single vortex having a constant vorticity distribution in the core, a Rankine vortex, is used here as the incident vortex that consists of multiple vortex elements free to move. A hybrid method composed of a random vortex method[8] and a vortex sheet method[9] are used to simulate the vorticity dominant flowfield generated from the surface of a wedge due to a viscous effect. The velocities of vortex particles both in the incident vortex and from the body surface to satisfy the no-slip boundary condition are calculated by using a fast vortex method.

This Euler-Lagrangian method requires only $\sim \mathcal{O}(N)$ computational time for N vortices, whereas $\sim \mathcal{O}(N^2)$ computational time is required for the direct discrete method using the Biot-Savart law. The vortex-in-cell method is a kind of fast vortex method and is used for free space[10] and vortex-airfoil interaction.[11] A more accurate method was developed recently and used in the calculations of flow induced by a vortex in free space[12] and flow in a driven cavity.[13] The method, originally developed for a rectangular grid, is applied here for vortex-wedge interaction by using a body-fitted coordinate transformation.

Governing Equations and Numerical Methods

The incompressible, unsteady, two-dimensional Navier-Stokes equations in the vorticity form are as follows:

$$\frac{\partial \xi}{\partial t} + (u \cdot \nabla)\xi = \frac{1}{Re} \nabla^2 \xi \tag{1a}$$

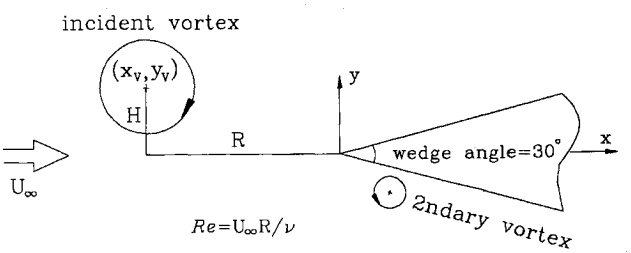

Fig. 1 Schematic diagram of vortex-wedge interaction (H and R are the initial position of an incident vortex).

Presented as Paper 90-3918 at the AIAA 13th Aeroacoustics Conference, Tallahassee, FL, Oct. 22-24, 1990; received May 8, 1991; revision received Nov. 29, 1993; accepted for publication Dec. 28, 1993.

*Graduate Student, Department of Aerospace Engineering, 373-1 Kusong-Dong Yusung-ku.

†Associate Professor, Department of Aerospace Engineering, 373-1 Kusong-Dong Yusung-ku. Member AIAA.

$$\nabla \cdot u = 0 \tag{1b}$$

where u is the velocity, ξ is the vorticity, and Re is the Reynolds number. The boundary conditions are zero tangential and normal velocities on the body surface.

The hybrid random vortex method that consists of the vortex sheet method and the random vortex method was developed to solve these equations for high Reynolds numbers.[8,9] This method has been applied to model a wide variety of viscous flow problems, including flow around an impulsively started cylinder,[14] flow past a backward-facing step,[15] and flow in a dump combuster.[16] A schematic diagram of these methods for vortex-wedge interaction is shown in Fig. 2. The vortex sheet method is used for flow near the body surface, where the boundary-layer assumption is valid. The random vortex method is used for flow outside the numerical boundary layer (which is thinner than the physical boundary layer) and also used near the leading edge of a wedge at which position the boundary-layer assumption fails because of the sharp curvature. At each time, vortex particles with a finite radius (called vortex blobs) or vortex sheets with a finite length are generated at the body surface to satisfy the no-slip boundary condition. These vortex elements are convected with local velocities.

The velocities of vortex blobs outside the numerical boundary layer are determined by using a fast vortex method. The velocities of vortex sheets inside the numerical boundary layer are determined from the approximate boundary-layer solutions. A random walk is, then, applied to each vortex sheet or the vortex blob to account for the diffusive effects of viscosity. The details of the methods are well described in Refs. 13, 14, and 17. The brief explanations of the methods are as follows.

Random Vortex Method

Equation (1a) can be considered as two fractional steps: an advection and a diffusion. The advection can be written in the inviscid Euler equation,

$$\frac{\partial \xi}{\partial t} + (u \cdot \nabla)\xi = 0 \tag{2a}$$

$$\nabla \cdot u = 0 \tag{2b}$$

The Euler equation is solved by using a vortex method with the boundary condition. In the vortex method, the vorticity field at time $n\Delta t$ is represented as a sum of discrete vortex particles with finite core radii, called vortex blobs:

$$\xi^n(x) = \sum_{j=1}^{N} K_\sigma(x_j^n - x)\Gamma_j \tag{3}$$

where K_σ is the cutoff function used to remove the singular behavior of a point vortex, Γ_j is the strength (or the circulation) of a vortex blob, and σ is the cutoff radius of the vortex blob.

Once the vorticity fields are determined, the vortex blobs move into the next time step positions with local velocities. In this study, the following second-order Runge-Kutta time integration scheme is used:

$$\begin{aligned} x_i^{n+1/2} &= x_i^n + \frac{\Delta t}{2} \cdot u_i(x_i^n) \\ x_i^{n+1} &= x_i^n + \Delta t \cdot u_i^{n+1/2}(x_i^{n+1/2}) \end{aligned} \tag{4}$$

where Δt is the time step, and i indicates the ith vortex blob. The velocities of the vortex blobs are calculated by using a fast vortex method. The method will be discussed later.

In a Lagrangian description (that is, when flow is described in terms of flow particles moving with convection velocities), Eq. (1a) can be written in the following diffusion equation:

$$\frac{\partial \xi}{\partial t} = \frac{1}{Re} \nabla^2 \xi \tag{5}$$

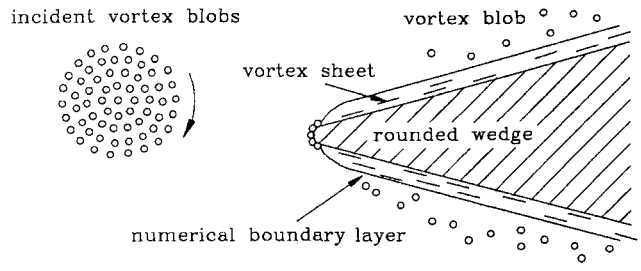

Fig. 2 Hybrid random vortex method for vortex-wedge interaction.

This implies that the kinematic viscosity causes the vorticity diffusion. The diffusion effect is statistically expressed by a random walk.[8,17] Then the final positions of vortex blobs are as follows:

$$x_i^{n+1} = (x_i^{n+1})_{\text{convection}} + \eta_i \tag{6}$$

where η is an independent Gaussian distributed random number with mean 0, and the variance is $2\Delta t/Re$.

Vortex Sheet Method

Where the boundary-layer assumptions are valid, Eqs. (1) can be approximated as Prandtl's boundary-layer equations:

$$\frac{\partial \xi}{\partial t} + (u \cdot \nabla)\xi = \frac{1}{Re} \frac{\partial^2 \xi}{\partial y^2} \tag{7a}$$

$$\xi = -\frac{\partial u}{\partial y} \tag{7b}$$

$$\nabla \cdot u = 0 \tag{7c}$$

where x and y denote an abscissa and an ordinate of the body-fitted coordinates, respectively. The no-slip and no-flow boundary conditions should be satisfied on the surface. The vortex sheet method is applied beneath the numerical boundary layer δ_{num} that is different from the physical boundary layer in reality. The thickness of the former is much smaller than that of the latter: If the numerical boundary is restricted to $\mathcal{O}(\sqrt{\Delta t/Re})$ for a small value of Δt and high Re number, the boundary-layer assumption can be used even if the flow outside the δ_{num} is not boundary-layer flow, i.e., the numerical boundary layer is merely a mechanism to allow sheets to exist that were generated at the surface or changed from blobs outside δ_{num}.

Let us define the vortex sheet strength as circulation per unit length of a vortex sheet, and this can be writen as follows:

$$\gamma_i = \lim_{\Delta y \to 0} \int_{y_i}^{y_i - \Delta y} \xi \, dy \tag{8}$$

Then, the vorticity at time $n\Delta t$ is represented by a sum of the linear concentrations of the discrete vortex sheet strengths:

$$\xi^n(x) = \sum_j \gamma_j b_h(x - x_j^n)\delta(y_j^n - y) \tag{9}$$

where γ_j is the strength of a vortex sheet (circulation/length, m/s), x_j, y_j is the vortex sheet center, δ is the Dirac delta function, and b_h is the smoothing function;

$$b_h(x) = \begin{cases} 1 - |x/h|, & |x| < h \\ 0, & \text{otherwise} \end{cases} \tag{10}$$

where h is the length of a vortex sheet. Then, the tangential velocity u is obtained from Eq. (7b) as

$$u_i^n(x, y) = U_\delta^n(x) + \sum_j \gamma_j b_h(x - x_j^n)H(y_j^n - y) \tag{11}$$

where H is the Heaviside function. The normal velocity v is obtained from Eq. (7c) as

$$v_i^n(x, y) = -\partial_x U_\delta^n(x) \cdot y - \frac{1}{h}\sum_j \gamma_j \left[b_h\left(x + \frac{h}{2} - x_j^n\right) - b_h\left(x - \frac{h}{2} - x_j^n\right)\right] \min(y, y_j^n) \tag{12}$$

The ith vortex sheet moves into the new position at $n+1$ time step as follows:

$$\begin{aligned} x_i^{n+1} &= x_i^n + \Delta t \cdot u_i \\ y_i^{n+1} &= y_i^n + \Delta t \cdot v_i + \eta_i \end{aligned} \tag{13}$$

Here, a random walk is applied in y direction only in these boundary-layer assumptions.

The no-slip boundary condition is satisfied as follows. The induced velocity $u(x)$ by freestream $U(x)$, vortex sheets, and blobs is calculated at each vortex sheet generation point on the wedge surface. If $|u(x)| > \gamma_{\max}$ (maximum allowable vortex sheet strength, one of the numerical parameters), then vortex sheets with each a finite length h and strength $\gamma(<\gamma_{\max})$ are generated at the surface of the wedge to satisfy the no-slip boundary condition. Here, multiple sheets are produced at each generation point to represent the boundary layer smoothly. The no-flow condition is satisfied on the surface as in Eq. (12). These vortex sheets are diffused and convected according to the previous equations.

A vortex sheet crossing the numerical boundary layer converts into a vortex blob whose strength is $\Gamma_i = \gamma_i h$.

Fast Vortex Method

The velocities of vortex blobs are determined by solving the following velocity Poisson equation:

$$\nabla^2 u(x) = -\nabla \times \xi k \cong \sum_{j=1}^{N} g_D(x - x_j) \tag{14}$$

where k denotes the unit vector of the vorticity in two dimensions. The source term g_D is the discrete Laplacian of the velocity field due to a point vortex.[12] In this calculation, the Scully vortex model,[18] which is differentiable, is used instead of a point vortex. The Scully vortex model is as follows:

$$v_\theta = \frac{\Gamma}{2\pi}\frac{r}{r^2 + a^2} \tag{15}$$

where a denotes the position of the maximum tangential velocity.

A nine-points finite difference Laplacian is used to obtain the source term g_D. The Possion equation is solved by using a fast Poisson solver on a grid system in the numerical domain. The image method is used to satisfy the normal boundary condition on the body surface in the numerical domain. The far-field boundary condition is calculated using the Biot-Savart law. Cubic spline interpolation is used in evaluating the velocities of vortex blobs located inside each grid point.

Implementation of the Methods

The incident Rankine vortex initially located in front of the wedge is modeled as multiple vortex elements as shown in Fig. 3. The vortex core is discretized in a way that causes no vortex instability[6]; i.e., each vortex element has an equal area, the center of each vortex is located in the centroid of the element, and the aspect ratio of the element $dr/r\,d\theta$ is almost 1.

A Schwarz-Christoffel transformation is used to generate a grid system and to relate the numerical domain (ζ) with the physical domain (z). A special method for rounding off the sharp leading edge of a wedge[19] is also employed in the transformation to avoid the singularity at the leading edge. The equation is

$$z = a\int [(\zeta - s_j)^{\alpha/\pi - 1} + (\zeta + s_j)^{\alpha/\pi - 1}]\, d\zeta + b \tag{16}$$

where α is the angle of a wedge, a and b are the constants related to the transformation, and s_j is the constant connected with the rounding off.

The velocity field calculated on the grid system in the numerical domain is transformed into the velocity in the physical domain as

$$V(z) = V(\zeta)\frac{d\zeta}{dz} \tag{17}$$

The trajectories of vortex blobs are calculated in the physical domain. Time integration should be carefully applied due to the existence of the numerical boundary layer, of which the above and below vortex blobs and sheets switch over. A second-order Runge-Kutta method with an elaborate algorithm is used for blobs, and a first-order Euler method is used for sheets. The new positions of the vortex blobs in the numerical domain are obtained from the physical positions by using the Newton method to solve the nonlinear equation of Eq. (16) at each time step.

Vortex blobs used in the calculation consist of three types: one from the incident vortex elements, another from vortex sheets crossing the numerical boundary layer, and the other from vortex particles generated directly near the leading edge of the wedge (refer to Fig. 2).

Random walks are applied to the vortex sheets or blobs generated at the surface but not for the incident vortex blobs. Vortex sheets or blobs that happened to be beneath the wall are reflected back into the flowfield. Vortex sheets or blobs beyond the calculation domain are automatically removed. The far-field boundary condition is easily acquired by using the Biot-Savart law.

Results and Discussion

The velocity and the space coordinate are nondimensionalized by U, the freestream velocity, and R, the distance from the center of the initial incident vortex and the leading edge of the wedge. The characteristic length used in the Reynolds number is R. Nondimensional time t is defined as $t = t^*U/R$, where t^* is a dimensional value. The strength of the incident vortex Γ is nondimensionalized by U and R and is taken as negative for the clockwise rotation (See Fig. 1).

Incident Vortex

The fast vortex method used in our calculation is verified by calculating the velocity field of the incident Rankine vortex. The strength is -1, and the radius of the Rankine vortex is 0.3. The grid size is 0.0625. The calculated velocity and the analytic one are compared in Fig. 4, which shows a good agreement between two results except the velocity near the core edge having discontinuous velocity gradient for the Rankine vortex.

Inviscid Interaction

A Rankine vortex is used to calculate the vortex-wedge interaction for a wedge with a 30-deg angle. In this case, the flow is assumed inviscid. The grid system used in this study is shown in Fig. 5.

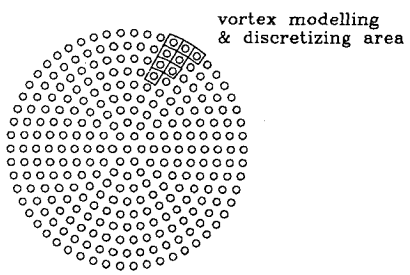

Fig. 3 Structures of incident vortex elements.

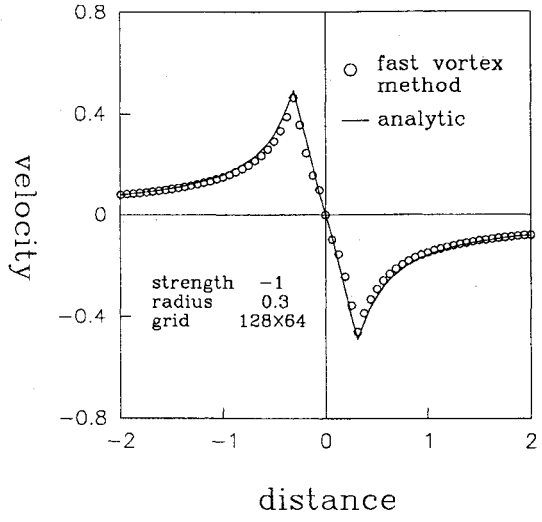

Fig. 4 Velocity profiles for the Rankine vortex in free space (strength $\Gamma = -1.0$, radius $R_v = 0.3$).

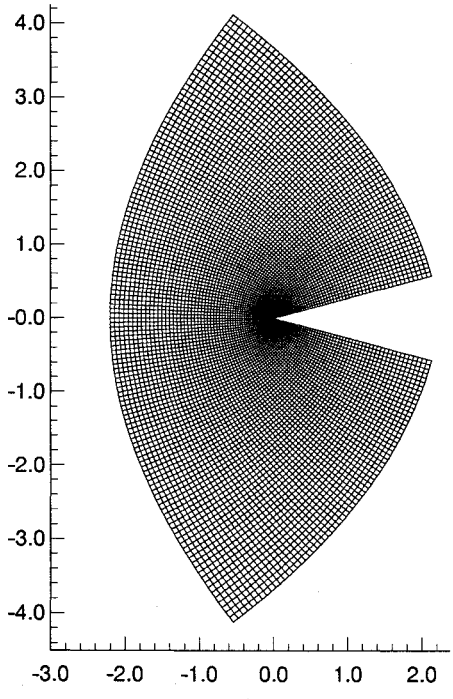

Fig. 5 Grid system (128 × 64).

First, we compared the solution obtained by using the fast vortex method with the one by the analytic method (i.e., the Biot-Savart law). The incident vortex used in this comparison is as follows: the strength Γ is -1.0; the radius R_v is 0.3; and the initial horizontal x_v and vertical position y_v is -1.0 and 0.15, respectively. Figure 6a shows split-incident vortex particles simulated by the fast vortex method and the analytic method at $t = 1.7$. Almost the same vortex patterns are obtained. Center positions of the incident vortex with time are plotted in Fig. 6b. A good accordance between two solutions is obtained. A second-order Runge-Kutta time integration described in Eq. (13) with $\Delta t = 0.01$ or 0.02 and 128×64 or 64×32 grid system is used for comparisons.

The effects of the initial vertical positions are calculated at $y_v = 0$, 0.15, and 0.3 for a vortex $\Gamma = -1$, and the corresponding vortex particles and streamlines are shown in Figs. 7a–7c, respectively. The radius and the initial horizontal position for the incident vortex are the same as in the previous case. For $y_v = 0$, it is clearly shown that the incident vortex initially located in the centerline dives into the lower side of the wedge. This "diving" behavior was found by Ziada and Rockwell[1] and is attributed to nonlinear interaction between an incident vortex and a wedge; as the rotational direction of the incident vortex is clockwise, by the mirror effect, the incident vortex itself tends to dive. For $y_v = 0.15$, the portion of the upper side-split vortex is more than that of $y_v = 0$. In the case of $y_v = 0.3$, the smaller part of the incident vortex moves into the lower side of the wedge. In this case, there exist the vortex blobs underneath the wedge, irrespective of the initial location of all of the vortex blobs in the incident vortex above the centerline. This is also due to the diving behavior during the interaction. In all three cases, the vortex particles in the lower side move close to the wedge surface, whereas the vortex particles in the upper side move away from the surface. In the streamlines in Fig. 7, it can be seen that the degree of perturbation on the upper and lower flowfield around the wedge varies according to the variation of y_v. It is observed that as y_v is lower, the portion and convection speed of the lower side of the split-incident vortex increases. This tendency is confirmed in the figures in Ziada and Rockwell.[1] However, a shed vortex, the result of viscous interaction between the incident vortex and the wedge, cannot be acquired in this calculation due to the limitation of the inviscid assumption.

Boundary-Layer Solution

The viscous effects are included by generating vortex sheets and/or vortex blobs at the body surface to meet the no-slip boundary condition and by applying random walks for the generated vortex sheets or blobs. To verify the hybrid random vortex method, we applied the method on the laminar boundary layer of a wedge with a 30-deg angle and compared it with the exact solution, the Falkner-Skan boundary-layer solution. In Fig. 8, the numerical result is time-averaged values over 60 time steps. In this case, the numerical boundary-layer thickness is about one-quarter of the physical boundary layer. Parameters used are as follows: $\Delta t = 0.05$; $\delta_{num} = 4\sigma$, where $\sigma = (2\Delta t/Re)^{1/2}$; $Re = 10^4$; γ_{max}(maximum allowable vortex sheet strength) = 0.05; and $h = 0.05$. Below $\eta = 1$, the vortex sheet method was applied. Above $\eta = 1$, the fast vortex method was used in calculating the convection velocities of blobs, whereas the Biot-Savart law was used to calculate a

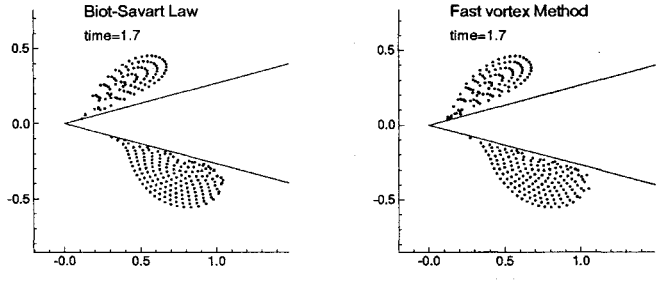

a) Vortex patterns at time = 1.7

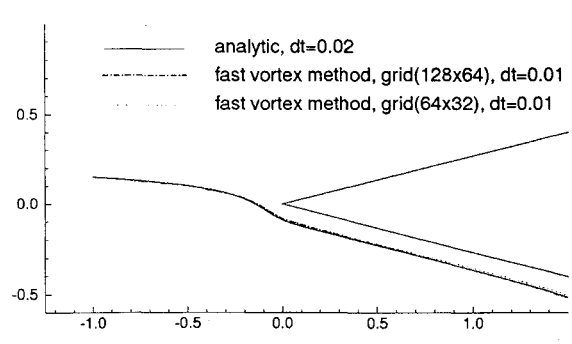

b) Trajectory of the vortex center (time = 0.0 ~ 2.5)

Fig. 6 Accuracy test for the fast vortex method.

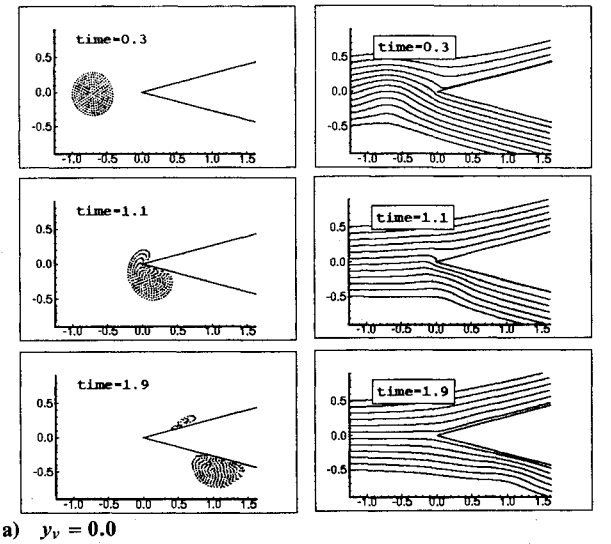

a) $y_v = 0.0$

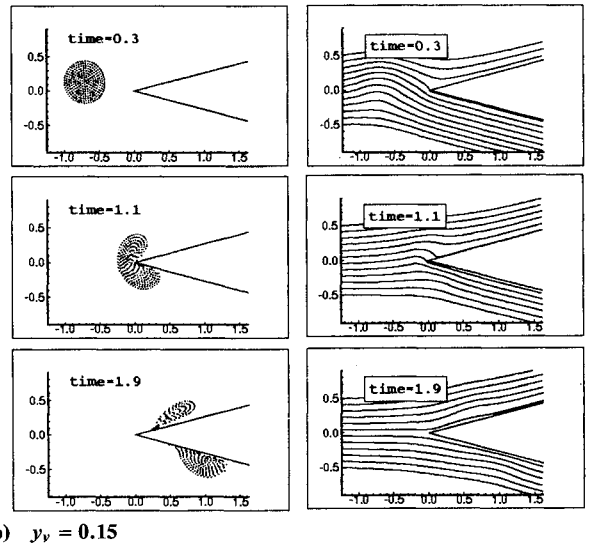

b) $y_v = 0.15$

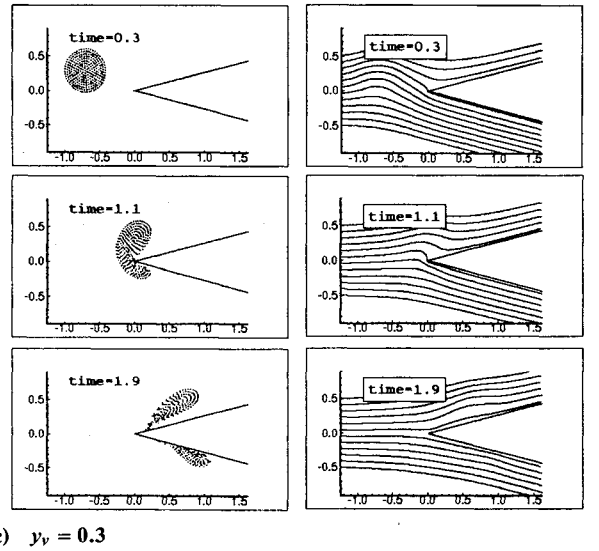

c) $y_v = 0.3$

Fig. 7 Effect of the initial vertical position y_v: inviscid interaction, $\Gamma = -1.0$.

similarity solution. Around $\eta = 1$, some errors occur, but the numerical solution accords well with the analytic solution on the whole.

Viscous Interaction

The same incident vortex ($\Gamma = -1$, $R_v = 0.3$, $x_v = -1$) is used as in the inviscid case, and the initial vertical position is fixed as $y_v = 0.15$ with $Re = 10^4$. The numerical parameters used in this calculation are as follows: $\Delta t = 0.01$, $\gamma_{max} = 0.05$, $h = 0.04$, $\delta_{num} \cong 2\sigma$; here, relatively small parameters were used to accurately describe the vortex dominant flowfield.

The incident and shed vortices, velocity vectors, and streamlines during the interaction are shown at selected times in Figs. 9a–9c, respectively. From now on, "a secondary vortex" refers to "a shed vortex." In Figs. 9a and 10, vortex blobs located above the numerical boundary are shown; however, vortex sheets near the surface are not shown. The number of vortices generated at the surface due to the viscous effect is larger than that of the incident vortex, because the former vortices are created at every time step to satisfy the no-slip boundary condition. As time passes by, a secondary (shed) vortex whose overall vorticity orientation is opposite to that of the incident vortex is growing up beneath the edge of the wedge and then comes off the edge at a certain time, convecting down along the wedge surface. The convection velocity of the shed vortex is slower than that of the incident vortex. It can be found in Figs. 9a and 9c that the boundary layers in the lower surface of the wedge are perturbed by the lower portion of the split-incident vortex. This phenomenon can also be found in the flow visualization figures by Ziada and Rockwell.[1] This is due to the perturbation by the clockwise rotating incident vortex.

The behaviors of the incident vortex seem similar to those of the inviscid case. Thus, the distortion and splitting of the incident vortex can be attributed almost to the inviscid interaction between the vortex and the wedge. The vortex blobs in the lower portion of the split-incident vortex pass over the strong secondary vortex, not mingling with it as in the experiment.[1] The flowfield around the wedge, the size and position of the secondary vortex with the lapse of time, is clearly shown in Figs. 9b and 9c. The flowfields around the lower surface of the wedge are perturbed by the strong secondary vortex unlike the inviscid case (compare Fig. 9c with Fig. 7b). This indicates that surface pressures will fluctuate considerably due to the secondary vortex.

Detailed secondary vortex structures at $t = 1.3$ and 1.7 are shown by the vortex particles and velocity vectors in Fig. 10a and the pictures of the vortex particles in Fig. 10b. In Fig. 10b, darker points represent counterclockwise rotating (plus-sign) vortices and brighter points clockwise rotating (minus-sign) vortices. At $t = 1.3$, a well-developed oval shape secondary vortex seems to be detached from the edge of the wedge. At $t = 1.7$, the fully developed circular shape secondary vortex is clearly identified, and the instabilities of the boundary layer around the vortex can be seen. At $t = 1.3$, most of the clockwise rotating vortices in the secondary vortex are gathered at

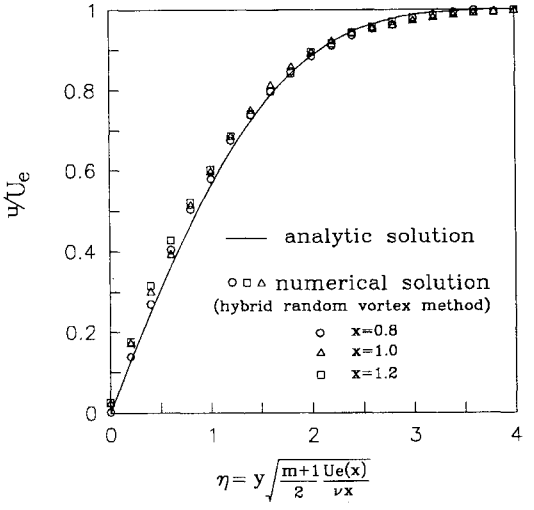

Fig. 8 Similarity solutions of laminar boundary layer over a wedge of angle 30 deg, $Re = 1.0 \times 10^4$ (x is the distance from the edge of the wedge).

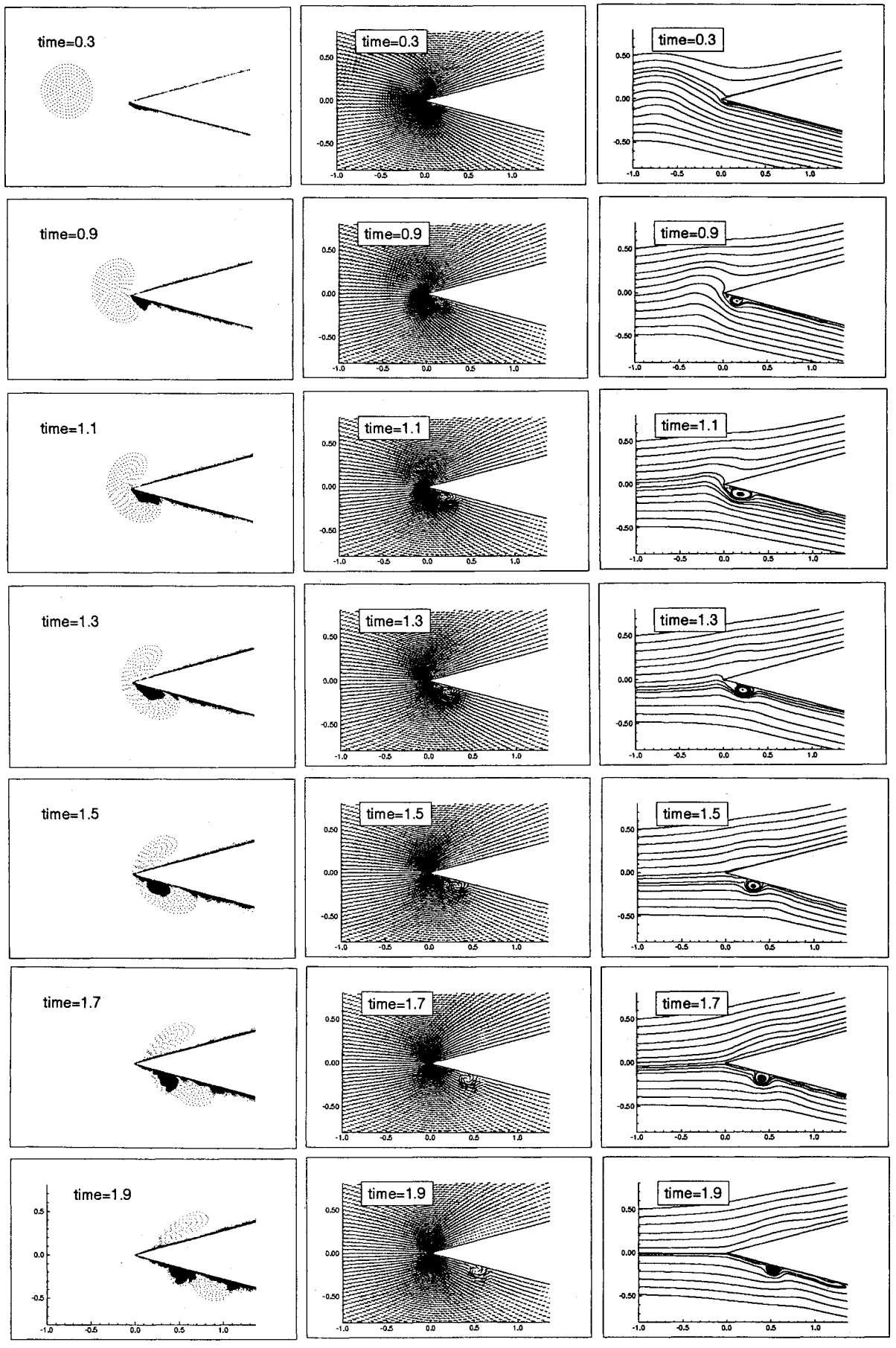

a) Vortex particle plots b) Velocity vectors c) Streamlines

Fig. 9 Viscous interaction ($\Gamma = -1.0$, $y_v = 0.15$), $Re = 1.0 \times 10^4$.

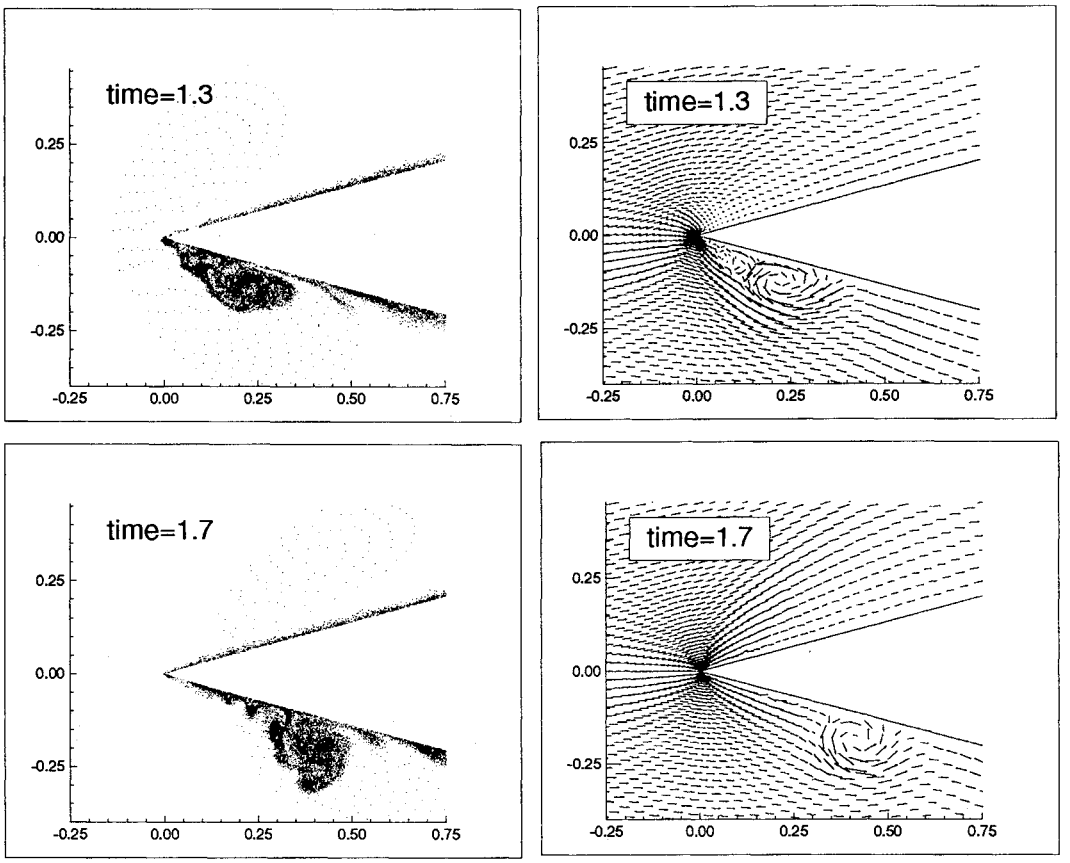

a) Vortex particle plots and velocity vectors

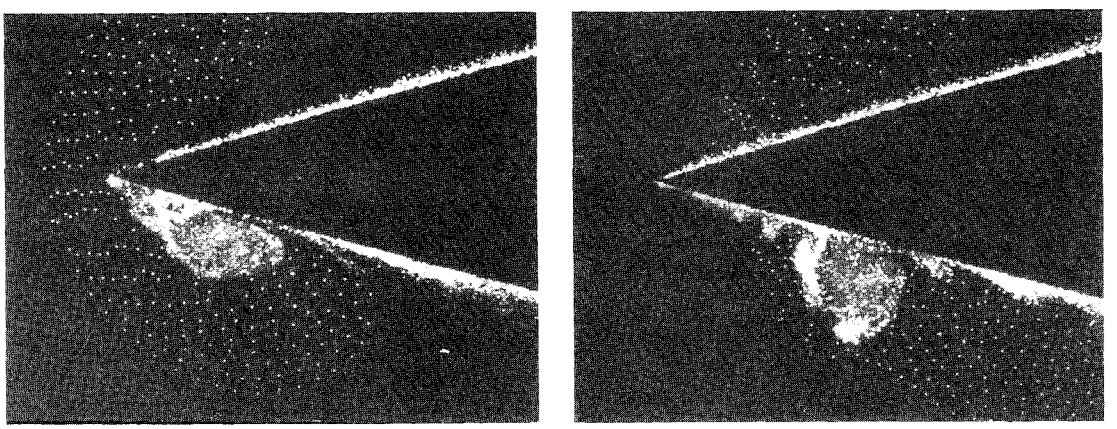

b) Black and white photographs of the vortex particles (bright point: clockwise rotating vortex, dark point: counterclockwise rotating vortex)

Fig. 10 Detailed structure of the secondary vortex.

the rear of the secondary vortex due to a strong reverse flow; similar phenomena can be found in Harvey and Perry,[20] Pauley et al.,[21] and Shih et al.[22] The number of minus-sign clockwise rotating vortices in the seconday vortex at $t = 1.7$ is more than that of the vortices at $t = 1.3$. Many of them are shifted by dominating plus-sign counterclockwise rotating vortices to the top of the secondary vortex. These increased minus-sign vortices that reside in the secondary vortex lead to the decay of the vortex strength itself. The vortex strength decay is explained in detail in the following paragraphs. The symptoms of a tertiary vortex at $t = 1.3$ can be found both in the velocity vectors and the picture (the appearance of a tertiary vortex was more evident as the strength of the incident vortex increased). The vortex structures at $t = 1.3$ are depicted schematically in Fig. 11.

Vortex origins can be identified if the wedge surface is partitioned into several parts and vortices generated from these regions are known. The results (related outputs are not included in this paper) are as follows: most of the vortices forming the secondary vortex are counterclockwise rotating vortices generated from the edge of the wedge, but the secondary vortex is contaminated continually by clockwise rotating vortices generated at the wall as the secondary vortex moves down along the surface (almost all of the brighter clockwise rotating vortices in Fig. 10 are generated at the wall, not from the edge of the wedge), and after $t = 1.3$, vortex shedding from the edge of the wedge ceases (this can also be confirmed in Fig. 9a). Thus, the leading edge of a wedge is very important to the interaction and noise generation.[1,2] Shih et al.[22] have also recognized the importance of the leading edge of an airfoil during unsteady motions.

The position and strength of the secondary vortex are quantified in Fig. 12. The secondary vortex position is quantified by simply identifying the center of the vortex in the streamline

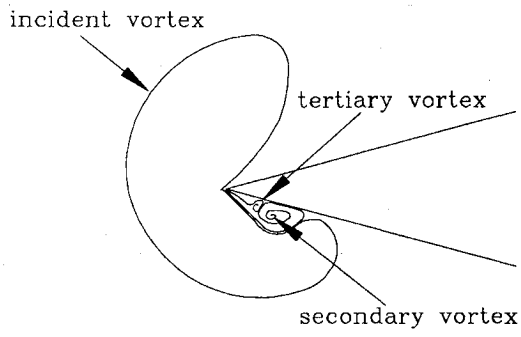

Fig. 11 Schematic diagram of the vortex structures at time = 1.3.

plots in Fig. 9 (the vortex center defined here may differ from the centroid of the vortex as defined by Shih et al.[22]). The quantification of strength is made by summation of each vortex strength resided in the secondary vortex area shown in vortex particle plots or streamline plots. The slope of x_{sec} (nondimensionalized distance of the secondary vortex position from the edge), i.e., dx_{sec}/dt, is almost linear and changes near t_{sep}. Here t_{sep} is defined as a separation time when the secondary vortex departs the edge of the wedge. Then, t_{sep} is estimated about 1.3 from the streamline plots and vortex particle plots in Fig. 9 and from this diagram. The estimated convection speed (normalized by the uniform flow) of the secondary vortex is about 0.15 before t_{sep} and about 0.50 after t_{sep}; i.e., the convection speed after t_{sep} is faster than before t_{sep} and is about one-half of the freestream velocity. The convection speed of the lower portion of the split-incident vortex is almost the same as the freestream velocity, 1.0.

From Fig. 12, it is clearly shown that the secondary vortex strength is directly related to its own convection velocity. The secondary vortex strength increases before t_{sep} and then slowly decreases with time. This explains one of the reasons for the difference of the slope curve dx_{sec}/dt before and after t_{sep}: Before t_{sep}, the secondary vortex raises its own vortex strength of which the energy is being supplied by the shear flow due to the nearing incident vortex; at this interval, the convection speed is relatively slower than after t_{sep}, due to its increasing strength; because the rotational direction of the secondary vortex is counterclockwise (positive), by the mirror effect (image vortex beneath the wall, clockwise rotation), the vortex itself moves toward the edge if the external uniform flow does not exist (its direction is from left to right).

The other effect influencing the slope curve dx_{sec}/dt is the lower and upper portion of the split-incident vortex (this portion is dependent on the initial position and strength of the incident vortex strength and on the freestream velocity and the wedge angle). The rotational direction of the lower portion of the split-incident vortex is clockwise, which increases the speed of the secondary vortex, and this induced velocity increases by the wall effect. Meanwhile, the upper portion of the split-incident vortex will decrease the speed of the secondary vortex. Thus the strength of the secondary vortex itself and the induced velocity by the lower and upper portion of the split-incident vortex are responsible for the convection speed of the secondary vortex.

Decay of the shed (secondary) vortex strength after t_{sep} is due to the interaction of the secondary vortex with the boundary layer at the wall. Similar phenomena on the strength decay of a vortex interacting with a two-dimensional boundary layer[23] or a three-dimensional boundary layer[24] have been experimentally observed. However, Barker and Crow[23] attributed the loss or periodic oscillation of strength to the finite core effect of the vortex. Shizawa and Eaton[24] have found that a longitudinal vortex interacting with a three-dimensional boundary layer loses its strength more rapidly than in a similar two-dimensional boundary layer.

The mechanism of the circulation loss was observed in our simulation as follows: The net sign of the vortices forming the secondary vortex are positive (counterclockwise) as seen in Fig. 12, which induces the upstream velocity at the lower surface (see Figs. 9b and 10). Then the vortices with a negative sign (clockwise) are generated at the surface to satisfy the no-slip condition. These negative-sign vortices mingle with the already existing secondary vortex composed mostly of positive-sign vortices generated from the leading edge, convecting down along the wall, decreasing the strength of the shed vortex itself after t_{sep} (refer to Fig. 10). Of course, due to the reverse flow by the secondary vortex (see Fig. 9, time = 0.9, 1.1), negative-sign vortices are also generated and mixed with the developing secondary vortex before t_{sep}, but as the number of positive-sign vortices exceeds that of negative-sign vortices due to the strong effect by the nearing incident vortex, the strength of the developing secondary vortex increases before t_{sep}.

Let us clarify the causes influencing the convection speed or similarly the position of the secondary vortex. Those are the strength and initial position of the incident vortex for a given freestream velocity and a wedge angle. These two factors determine the portion of the upper and lower side of the split-incident vortex and the secondary vortex strength. Finally, the portion of the split-incident vortex and the secondary vortex strength itself are responsible for its own convection velocity. The secondary vortex strength is found to change with time: it increases almost linearly before t_{sep} and then decreases due to a secondary vortex/boundary-layer interaction.

Quantitative comparisons of two results between the experiment of Ziada and Rockwell[1] and our numerical simulation are not presented because of the following differentiae: Reynolds number, modeling of shear layer by a Rankine vortex, and starting of the numerical simulation from the inviscid flow. Nevertheless, the numerical experiment could well reproduce the main features of vortex-wedge interaction: distortion and splitting of the incident vortex, vortex shedding near the leading edge, and the instabilities of the boundary layer in the lower surface of the wedge. Moreover, the initial development of a secondary vortex, the convection velocity change of the secondary vortex when it departs the leading edge of the wedge, and the timewise change of the secondary vortex strength and its relation to the convection speed of the secondary vortex are well presented by our numerical simulation. By the extension of this research, something can be considered: Reynolds number changes, variations of the initial vertical position of an incident vortex as in the experiment,[1] changes of an incident vortex strength, and more realistic modeling of shear layer, etc.

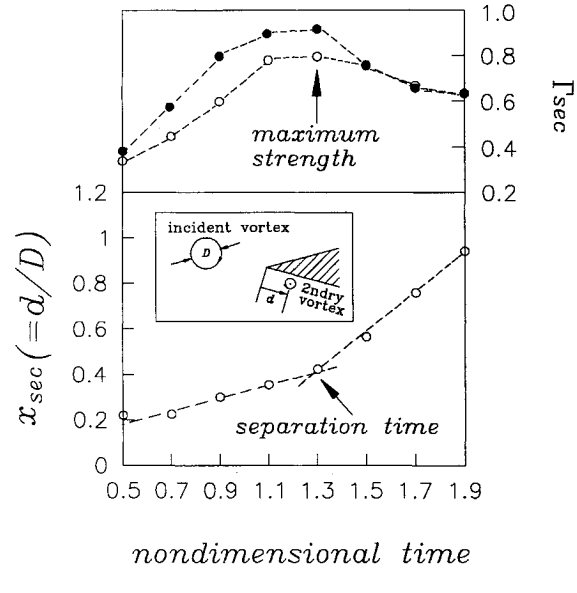

Fig. 12 Secondary vortex position from the edge of the wedge and the vortex strength with time, D = 0.6 (diameter of the incident vortex): ●, measured using vortex particle plots; ○, measured using streamlines.

Conclusions

Vortex-wedge interaction is simulated by using the hybrid random vortex method and a fast vortex method. Thus, the viscous effects are included, and a large number of vortex particles generated along the body surface can be taken into account. The initial vertical position of the incident vortex is located above the centerline of the wedge, at which a significant nonlinear interaction occurs and a strong secondary vortex is shed from the leading edge toward the underside of the wedge. The strength of the secondary vortex is less than that of the incident vortex and its vorticity orientation is opposite to that of the incident vortex. Distortion and splitting of the incident vortex during the interaction are mainly due to inviscid interaction, and the appearance of a shed vortex is attributed to viscous interaction. The convection speed and strength of the shed vortex are calculated. The strength of the shed vortex after it is detached from the leading edge decreases as time passes by due to its interaction with the boundary layer at the wall. The secondary vortex strength and the lower and upper portion of the split-incident vortex are responsible for the convection speed of the shed vortex itself for a given strength and the initial position of the incident vortex.

References

[1]Ziada, S., and Rockwell, D., "Vortex-Leading Edge Interaction," *Journal of Fluid Mechanics,* Vol. 118, May 1982, pp. 79–107.

[2]Rockwell, D., "Oscillations of Impinging Shear Layers," *AIAA Journal,* Vol. 21, No. 5, 1983, pp. 645–664.

[3]Rockwell, D., and Knisely, C., "The Organized Nature of Flow Impingment upon a Corner," *Journal of Fluid Mechanics,* Vol. 93, Pt. 3, 1979, pp. 413–432.

[4]Conlisk, A. T., and Rockwell, D., "Modeling of Vortex-Corner Interaction Using Point Vortices," *Physics of Fluids,* Vol. 24, No. 12, 1981, pp. 2133–2142.

[5]Conlisk, A. T., and Veley, D., "The Generation of Noise in Impinging Vortex Motion Past a Step," *Physics of Fluids,* Vol. 28, No. 1, 1985, pp. 3004–3012.

[6]Lee, D. J., "Surface Pressure Fluctuations Due to Impinging Vortical Flows upon an Airfoil," AIAA Paper 88-3657-CP, July 1988.

[7]Lee, D. J., and Smith, C. A., "Effect of Vortex Core Distortion on Blade-Vortex Interaction," *AIAA Journal,* Vol. 29, No. 9, 1991, pp. 1355–1362.

[8]Chorin, A. J., "Numerical Study of Slightly Viscous Flow," *Journal of Fluid Mechanics,* Vol. 57, Pt. 4, 1973, pp. 785–796.

[9]Chorin, A. J., "Vortex Sheet Approximation of Boundary Layers," *Journal of Computational Physics,* Vol. 27, No. 3, 1978, pp. 428–442.

[10]Christiansen, J. P., "Numerical Simulation of Hydrodynamics by the Method of Point Vortices," *Journal of Computational Physics,* Vol. 13, No. 3, 1973, pp. 363–379.

[11]Lee, D. J., and Chae, K. S., "Calculation of Vortex-Airfoil-Interaction by Using a Vortex-In-Cell Method," *Proceedings of the 27th Aircraft Symposium,* edited by K. Kondo, Kyushu Univ., Japan, 1989, pp. 574–577.

[12]Anderson, C. R., "A Method of Local Corrections for Computing the Velocity Field Due to a Distribution of Vortex Blobs," *Journal of Computational Physics,* Vol. 62, No. 1, 1986, pp. 111–123.

[13]Baden, S., and Puckett, E., "A Fast Vortex Code for Computing 2D Viscous Flow," *Journal of Computational Physics,* Vol. 91, No. 2, 1990, pp. 278–297.

[14]Cheer, A. Y., "Unsteady Separated Wake Behind an Impulsively Started Cylinder in Slightly Viscous Fluid," *Journal of Fluid Mechanics,* Vol. 201, April 1989, pp. 485–505.

[15]Ghoniem, A. F., and Gagon, Y., "Vortex Simulation of Laminar Recirculating Flow," *Journal of Computational Physics,* Vol. 68, No. 2, 1987, pp. 346–377.

[16]Najm, H. N., and Ghoniem, A. F., "Numerical Simulation of the Convective Instability in a Dump Combuster," *AIAA Journal,* Vol. 29, No. 6, 1991, pp. 911–919.

[17]Ghoniem, A. F., and Sherman, F. S., "Grid-Free Simulation of Diffusion Using Random Walk Methods," *Journal of Computational Physics,* Vol. 61, No. 1, 1985, pp. 1–37.

[18]Stremel, P. M., "Aerodynamic Interaction Between Vortical Wakes and the Viscous Flow About a Circular Cylinder," AIAA Paper 85-4063, Oct. 1985.

[19]Carrier, G. F., Krook, M., and Pearson, C. E., *Functions of a Complex Variable,* McGraw-Hill, New York, 1966.

[20]Harvey, J. K., and Perry, F. J., "Flowfield Produced by Trailing Vortices in the Vicinity of the Ground," *AIAA Journal,* Vol. 9, No. 8, 1971, pp. 1659, 1660.

[21]Pauley, L. L., Moin, P., and Reynolds, W. C., "The Instability of Two-Dimensional Laminar Separation," *Proceedings of the Conference on Low Reynolds Number Aerodynamics,* edited by T. A. Mueller, Vol. 54, Lecture Notes in Engineering, Springer-Verlag, Berlin, 1989, pp. 82–92.

[22]Shih, C., Lourenco, L., Van Dommelen, L., and Krothapalli, A., "Unsteady Flow Past an Airfoil Pitching at a Constant Rate," *AIAA Journal,* Vol. 30, No. 5, 1992, pp. 1153–1161.

[23]Barker, S. J., and Crow, S. C., "The Motion of Two-Dimensional Vortex Pairs in a Ground Effect," *Journal of Fluid Mechanics,* Vol. 82, Pt. 4, 1977, pp. 659–671.

[24]Shizawa, T., and Eaton, J. K., "Interaction of a Longitudinal Vortex with a Three-Dimensional, Turbulent Boundary Layer," *AIAA Journal,* Vol. 30, No. 5, 1992, pp. 1180, 1181.